Cell Stem Cell

Lymphangiocrine signals are required for proper intestinal repair after cytotoxic injury

Graphical abstract
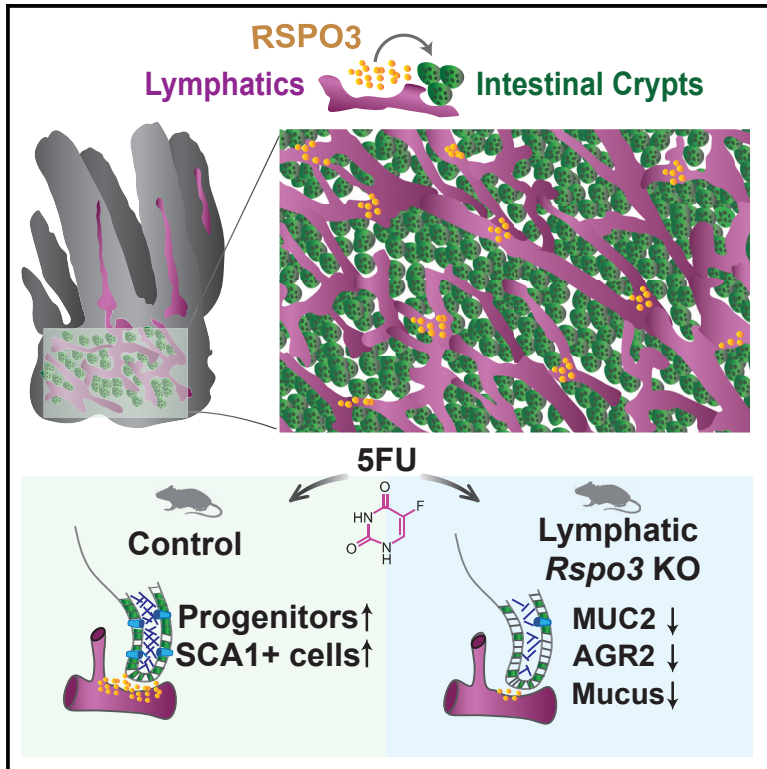
Authors

Brisa Palikuqi, Jérémie Rispal,
Efren A. Reyes, Dedeepya Vaka,
Dario Boffelli, Ophir Klein

Correspondence

ophir.klein@ucsf.edu

In brief

Palikuqi et al. employ imaging of cleared intestinal tissue, transcriptional analyses, and genetic mouse models to investigate the role of lymphatic endothelial cells in the intestinal stem cell niche. The authors demonstrate that lymphatic endothelial cells are an essential source of *Rspo3* for proper intestinal recovery after cytotoxic injury.

Highlights

- Intestinal crypts are in proximity to lymphatics, which express *Rspo3*

- Intestinal recovery is impaired in lymphatic *Rspo3* knockout mice after 5FU injury

- Lymphatic *Rspo3* knockout mice have decreased progenitor cells after 5FU injury

- Lymphatic *Rspo3* knockout mice have reduced mucus production after 5FU injury

CellPress

Short Article

Lymphangiocrine signals are required for proper intestinal repair after cytotoxic injury

Brisa Palikuqi,[1,6] Jérémie Rispal,[1,6] Efren A. Reyes,[1,2] Dedeepya Vaka,[3] Dario Boffelli,[3,4,5] and Ophir Klein[1,3,4,5,7,*]

[1]Program in Craniofacial Biology and Department of Orofacial Sciences, University of California, San Francisco, San Francisco, CA 94143, USA
[2]Department of Pharmaceutical Chemistry and TETRAD Program, University of California, San Francisco, San Francisco, CA, USA
[3]Institute for Human Genetics, University of California, San Francisco, San Francisco, CA 94158, USA
[4]Department of Pediatrics, University of California, San Francisco, San Francisco, CA 94158, USA
[5]Department of Pediatrics, Cedars-Sinai Medical Center, Los Angeles, CA 90048, USA
[6]These authors contributed equally
[7]Lead contact
*Correspondence: ophir.klein@ucsf.edu
https://doi.org/10.1016/j.stem.2022.07.007

SUMMARY

The intestinal epithelium undergoes continuous renewal and has an exceptional capacity to regenerate after injury. Maintenance and proliferation of intestinal stem cells (ISCs) are regulated by their surrounding niche, largely through Wnt signaling. However, it remains unclear which niche cells produce signals during different injury states, and the role of endothelial cells (ECs) as a component of the ISC niche during homeostasis and after injury has been underappreciated. Here, we show that lymphatic endothelial cells (LECs) reside in proximity to crypt epithelial cells and secrete molecules that support epithelial renewal and repair. LECs are an essential source of Wnt signaling in the small intestine, as loss of LEC-derived *Rspo3* leads to a lower number of stem and progenitor cells and hinders recovery after cytotoxic injury. Together, our findings identify LECs as an essential niche component for optimal intestinal recovery after cytotoxic injury.

INTRODUCTION

Enteric blood and lymphatic networks are intimately associated with the small intestinal epithelium, including the intestinal stem cells (ISCs) that reside in epithelial invaginations called crypts (Bernier-Latmani et al., 2015; Bernier-Latmani and Petrova, 2017; Beumer and Clevers, 2020; Cifarelli and Eichmann, 2019). Over the last decade, several groups have shown that paracrine factors secreted by endothelial cells (ECs) lining blood and lymphatic vessels, known as angiocrine factors, are important for stem cell maintenance and regeneration in many tissues (Augustin and Koh, 2017; Rafii et al., 2016). Blood ECs (BECs) play a central role in the regeneration of several organs, such as liver, lung, bone marrow, and thymus (Butler et al., 2010; Ding et al., 2010, 2011, 2012; Hu et al., 2014; Wertheimer et al., 2018). Notably, lymphatic ECs (LECs), through the secretion of the lymphangiocrine factor Reelin (RELN), have been linked to heart regeneration (Liu et al., 2020). In addition, the interaction of stem cells with LECs regulates stem cell cycling in the skin (Gur-Cohen et al., 2019). However, the role of intestinal ECs in ISC self-renewal and regeneration remains undetermined.

ISCs, which are marked by *Lgr5*, and their transit-amplifying descendants self-renew and differentiate along the various intestinal epithelial lineages (Barker et al., 2007; Gehart and Clevers, 2019). Maintenance of ISCs is dependent on the niche,

which is comprised of several cell types and is an essential source of Wnt ligands and modulators (McCarthy et al., 2020a; Palikuqi et al., 2021). Among these molecules, R-spondins (RSPOs), which bind to LGRs (LGR4 and LGR5 in the intestine), potentiate Wnt signaling (de Lau et al., 2011; Glinka et al., 2011) by stabilizing Frizzled receptors (Hao et al., 2012). RSPOs are essential for the expansion and renewal of ISCs both *in vivo* (Yan et al., 2017) and *in vitro* (Sato et al., 2009). RSPO3 is the predominant RSPO in the small intestine (Ogasawara et al., 2018), and inhibition of RSPO3, along with RSPO2 with a neutralizing antibody, negatively affects epithelial regeneration after irradiation (Storm et al., 2015).

Several mesenchymal populations have been reported to be essential sources of Wnt ligands and modulators in the intestine (Degirmenci et al., 2018; Kabiri, 2014; McCarthy et al., 2020b; Stzepourginski et al., 2017; Valenta et al., 2016). For instance, mesenchymal cells marked by *Foxl1*^{+}, known as telocytes, express high levels of *Wnt2* and *Wnt5a* (Aoki et al., 2016; Kondo and Kaestner, 2019; Shoshkes-Carmel et al., 2018). The inhibition of Wnt ligand secretion by deletion of *Porcupine* (*Porcn*) in *Foxl1*^{+} telocytes results in rapid stem and progenitor cell loss (Shoshkes-Carmel et al., 2018). Another subtype of mesenchymal cells, known as trophocytes and marked by expression of *Grem1* and *Cd81* and low expression of *Pdgfra*, resides in proximity to ISCs and expresses the Wnt family member *Wnt2b* as well as high levels of all R-spondins. Ablation of the

trophocyte mesenchymal population leads to loss of $Lgr5^+$ cells, while the population of transit-amplifying (TA) cells remains stable (McCarthy et al., 2020b). Moreover, deletion of *Rspo3* in *Pdgfra*$^+$ cells does not have a major effect on epithelial cells during homeostasis (Greicius et al., 2018), suggesting that this essential signal is produced by several different niche cell types.

LECs express high levels of *Rspo3* (Kalucka et al., 2020; Ogasawara et al., 2018), but it is unknown whether LECs are an essential source of Wnt signaling in the small intestine during homeostasis or injury. Additionally, while several lines of evidence suggest that ECs become activated and start proliferating in response to intestinal injury to drive epithelial recovery (Abel et al., 2005; Kinchen et al., 2018; Paris et al., 2001; Rehal et al., 2018), the contribution of ECs and, specifically, LECs to intestinal maintenance and repair remains an open question. Here, we establish the spatial organization of lymphatic vessels in relation to crypt cells and utilize single-cell RNA sequencing (scRNA-seq) to uncover the transcriptional composition of LECs, both during homeostasis and after cytotoxic injury. Using mouse genetics, we show that LEC-secreted *Rspo3* is essential for optimal intestinal repair after cytotoxic injury, positioning LECs as a key component of the intestinal niche and a critical source of Wnt signaling.

RESULTS

LECs reside in proximity to crypt cells

We first set out to delineate the location and molecular composition of LECs in the small intestinal niche. We utilized the CUBIC clearing method (Matsumoto et al., 2019), paired with whole-mount imaging, to determine the spatial distribution of LECs in the mouse small intestine during homeostasis and to establish the relationship of LECs to BECs and mesenchymal cells in the niche (Figures 1A, 1B, S1A, and S1B). VECAD$^+$ BECs and PDGFRA$^+$ mesenchymal cells surrounded every crypt (Figures 1B and S1A), but lymphatic vessels displayed a unique pattern of organization. We found two distinct sets of lymphatic vessels: large lymphatic vessels that encircled the base of the crypts and gave rise to narrow lymphatic vessels in the villi, known as lacteals (Figures 1A, 1B, S1A, and S1B). To determine the proximity of LECs to $Lgr5^+$ stem cells in the crypts, we performed whole-mount imaging on cleared small intestinal tissue from $Lgr5^{GFP-CreER}$ mice. LECs were in proximity to $Lgr5^+$ crypt cells at the base of the crypts and at the mid-crypt level (Figures 1C and S1C). More than 80% of crypts were in proximity to lymphatics at the base and/or mid-crypt levels, with 36% of crypts in proximity to LECs only at the base, 23% only at the mid-crypt region, and 26% at both (Figure 1D).

LECs express high levels of *Rspo3*

Next, we set out to establish the molecular composition of LECs in the small intestine by performing scRNA-seq. BECs and LECs were enriched by fluorescence-activated cell sorting (FACS) from the small intestine of wild-type mice and identified as CDH5$^+$, PODOPLANIN (PDPN)^{Neg} and CDH5$^+$, PDPN$^+$ cells, respectively (Figures 2A and 2B). In all, 6,000 BECs and 2,000 LECs were captured by scRNA-seq, with BECs clustering in 13 groups and LECs clustering in 2 groups (Figure 2C). LECs could be distinguished from BECs by the high expression *Lyve1* and

Pdpn (Figure 2D). Clustering was similar among 4 different mice in 2 separate experiments (Figure S1D). Notably, LECs uniquely expressed high levels *of Aqp1, Cyp4b1, Il33,* and *Mmrn1* genes compared to BECs (Figure S1E). The transcription factor *Maf* was also selectively expressed in LECs (Figure S1E). *Reelin* (RELN), which is expressed in the heart by LECs and has been found to be essential for heart regeneration, was also highly expressed by LECs, but not BECs, in the small intestine (Figure S1E).

As Wnt signaling is essential for ISC maintenance and proliferation, we mined the scRNA-seq data for the expression of Wnt family members. As previously reported (Kalucka et al., 2020; Ogasawara et al., 2018), LECs in the small intestine expressed high levels of *Rspo3* (Figures 2E and S1F). Additionally, LECs expressed high levels of *Wntless* (*Wls*, essential for the secretion of Wnt ligands) and the canonical Wnt family member *Wnt2* (Figures 2E and S1F). Interestingly, *Rspo3* and *Wnt2* were uniquely expressed by LECs, whereas *Wls* was also expressed by BECs (Figures 2E and S1F). *Rspo3* expression by LECs in proximity to epithelial crypt cells was confirmed by *in situ* hybridization (RNAscope) (Figure 2F); no other Wnt family members were expressed by LECs during homeostasis.

Loss of lymphatic *Rspo3* leads to impaired intestinal recovery after cytotoxic injury

As *Rspo3* is important for the proliferation of stem and progenitor cells in the crypt, we next utilized a genetic model to specifically delete *Rspo3* in LECs. We bred mice carrying the lymphatic driver *Prox1*^{CreER} with *Rspo3*$^{fl/fl}$ mice to generate *Prox1*^{CreERT2}; *Rspo3*$^{fl/fl}$ mice (Figure 3A). Deletion of *Rspo3* in adult LECs did not significantly alter crypts in the small intestine during homeostasis. Control and knockout mice had similar levels of EdU incorporation, crypt number, and OLFM4 expression after tamoxifen induction (Figures 3B–3E). Thus, during homeostasis, Wnt signaling from other, redundant niche components, such as PDGFRA$^+$ cells, is sufficient for ISC maintenance.

We then assessed whether lymphatic *Rspo3* is essential for intestinal recovery after injury, when crypt epithelial cells must undergo high proliferation. To test this hypothesis, we utilized 5-fluorouracil (5FU), a chemotherapeutic that selectively kills proliferating cells. Control and *Rspo3* knockout mice underwent sublethal 5FU injury and were sacrificed at day 3 after the last 5FU injection (Figures 3F and S2A). Sustained deletion of *Rspo3* after injury was confirmed by qPCR (Figure 3G). After 5FU injury, control crypt epithelium exhibited high levels of proliferation as measured by EdU incorporation, but knockout mice had significantly decreased proliferation (Figures 3H and 3I). The total number of regenerating crypts was significantly reduced in knockout mice (Figure 3J). Additionally, we quantified the size of crypts after 5FU and determined that, in knockout mice, crypts in proximity to LECs were decreased in size more than those not close to LECs (Figure 3K). The total levels of *Lgr5* mRNA and OLFM4 protein were also decreased in knockout crypt cells (Figures 3L–3O). Lastly, we asked whether loss of *Rspo3* resulted in structural changes in LECs after 5FU injury. LEC density and percentage of crypts found in proximity to LECs were similar in control and knockout mice, suggesting that changes in crypt cells after 5FU were due to lymphangiogrine signaling rather than to loss of LEC structures (Figures S2B–S2D).
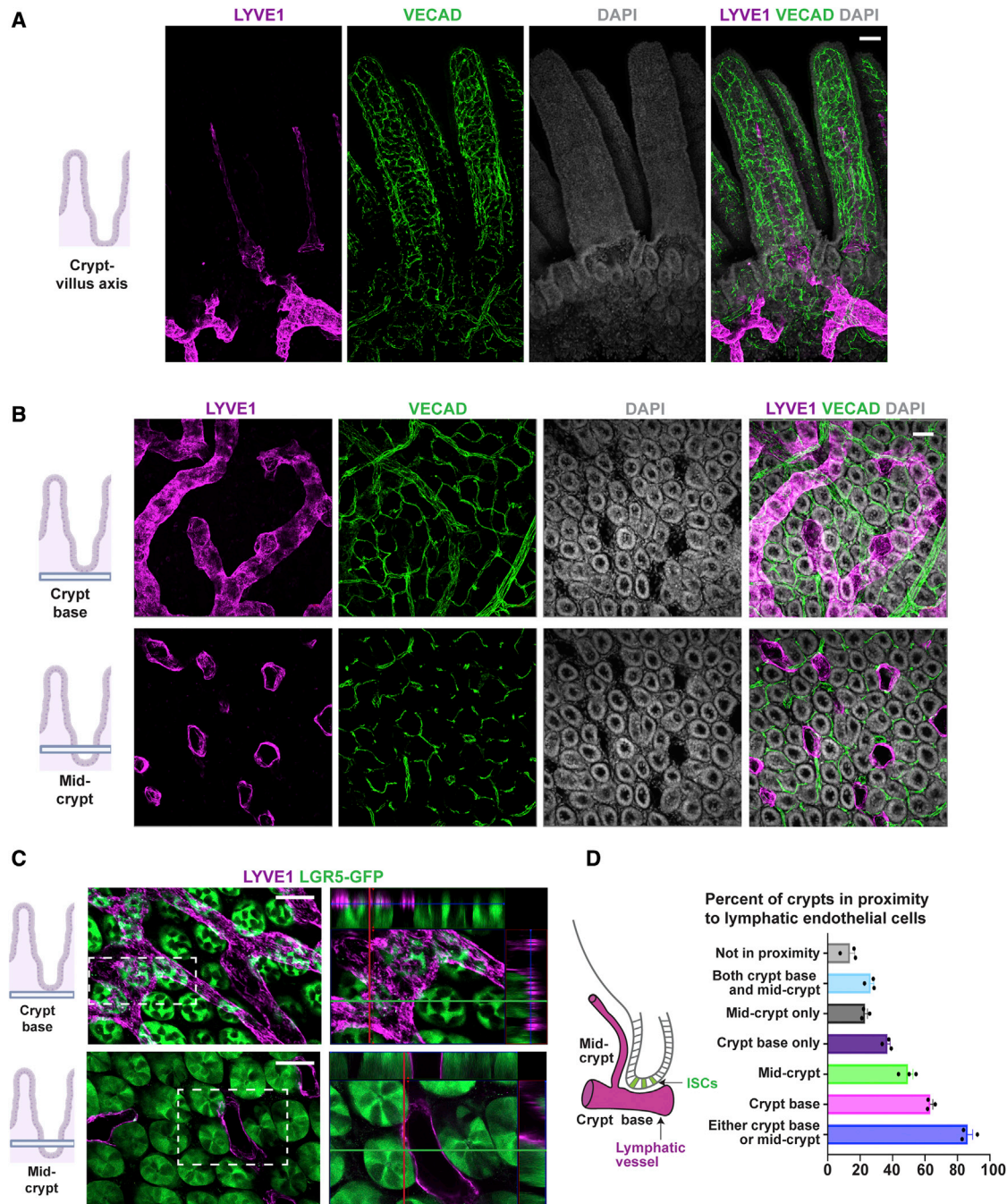
Figure 1. LECs reside in proximity to crypt cells

(A) Sagittal view of whole-mount imaging of CUBIC-cleared tissue from adult wild-type mouse small intestine stained for LYVE1 and VECAD showing the localization of lymphatic and blood vessels within the crypt-villus axis in the small intestine.

(B and C) Transverse view of LYVE1 and VECAD showing (B) the organization of LECs and BECs at both the crypt base region and mid-crypt region in adult wild-type mice and (C) the LECs proximity to $Lgr5^+$ ISCs in adult $Lgr5^{GFP-Cre}$ mice. Insets represent orthogonal projections of the whole mounts depicting adjacency and at times contact of LECs to $Lgr5^+$ ISCs.

(D) Left: schematic representation of position of lymphatic vessels in relation to crypts. Right: quantification of percentage of crypts in vicinity to LECs at the base of the crypts, at mid-crypt level, or not in proximity to any LECs (n = 3 mice). Scale bars, 50 μm.

See also Figure S1.
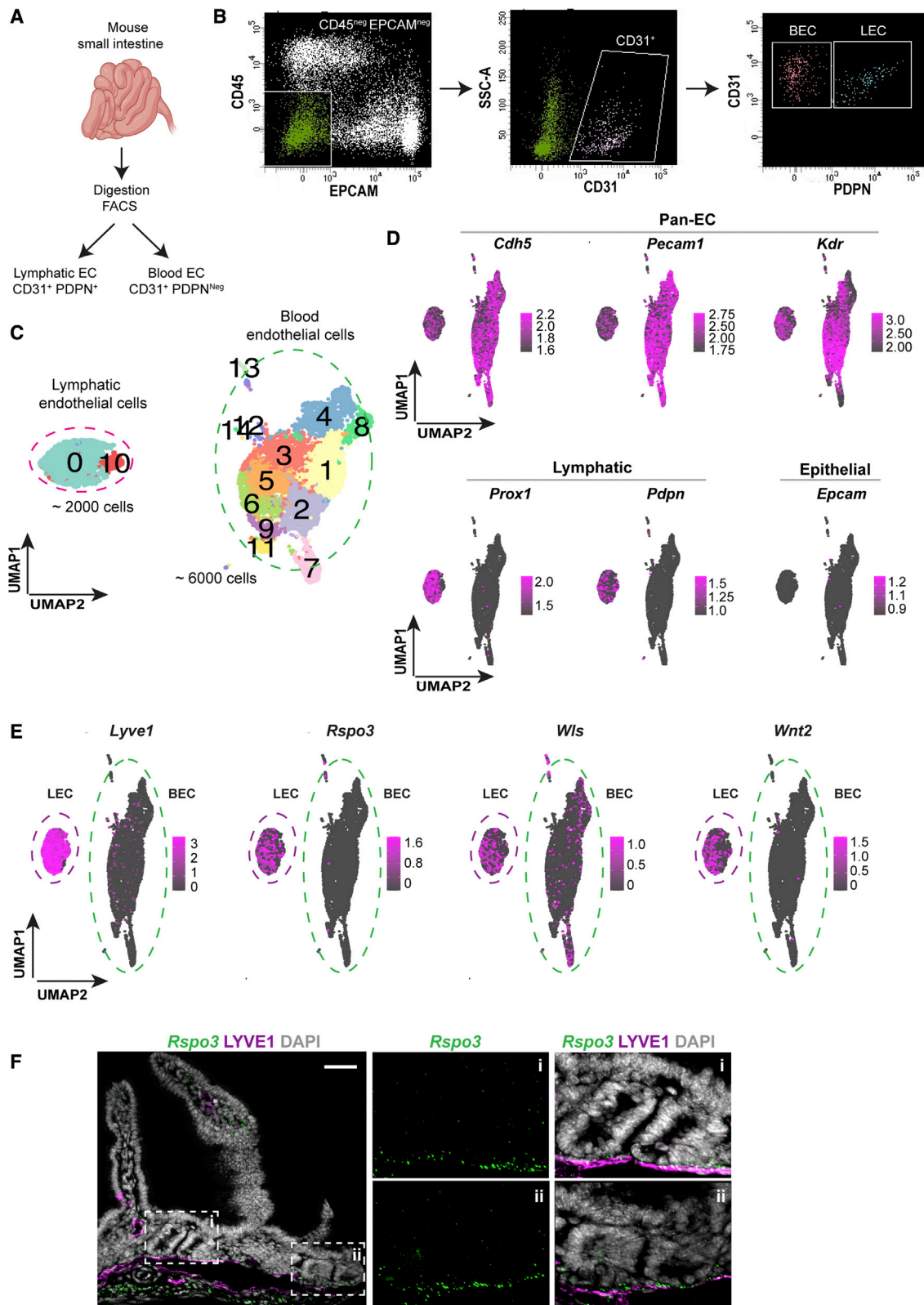
Figure 2. LEC scRNA-seq data reveal expression of *Rspo3* and other Wnt signaling molecules

(A) Small intestines from 4 wild-type mice in 2 independent experiments were digested, and LECs and BECs were isolated by sorting CD31$^+$, PDPN$^+$ and CD31$^+$, PDPN^{Neg} cells, respectively.

(legend continued on next page)

5FU treatment induces substantial damage to proliferating cells, potentially affecting both epithelial and niche cells. We therefore investigated whether a similar requirement for LEC-derived *Rspo3* exists when *Lgr5*⁺ cells alone are ablated. We bred *Prox1*^CreERT2;*Rspo3*^fl/fl;*Lgr5*^DTR mice, in which tamoxifen injection leads to deletion of *Rspo3* in LECs, and diphtheria toxin (DT) (Tian et al., 2011) injection results in ablation of *Lgr5*⁺ cells. Tamoxifen induction was followed by *Lgr5*⁺ cell ablation for 3 consecutive days (Figure S2E). Although there was a slight decrease in levels of proliferation as measured by EdU incorporation, the effect was less pronounced compared with that observed after cytotoxic injury (Figures S2F–S2J). Thus, LEC-derived *Rspo3* is essential for adequate intestinal recovery when there is a requirement for a marked increase in proliferation of epithelial cells and when the niche becomes activated during injury.

Loss of lymphatic *Rspo3* results in lower TA and *Sca1*^high cells after cytotoxic injury

Next, we set out to further uncover molecular changes in *Prox1*^CreERT2;*Rspo3*^fl/fl knockout mice after 5FU injury. At day 3 after the final 5FU injection, we isolated the following from both control and knockout mice: crypt epithelial cells as EPCAM⁺, CD44⁺; LECs as CD31⁺, PDPN⁺; BECs as CD31⁺, PDPN^neg; and other stromal cells as EPCAM^neg, CD31^neg. We then performed scRNA-seq on these cells (Figures 4A and S3A). Analysis included cells from two biological replicates with a total of 20,803 cells for control mice and 9,153 for knockout mice, with cells grouping in 29 clusters (Figures 4B and S3B). Clustering patterns were similar among the two experiments (Figure S3B). Crypt epithelial cells were identified as *Epcam*⁺, *Cd44*⁺, and LECs were identified by the pan-endothelial markers *Cd31*, *Cdh5*, or *Kdr* and expression of *Lyve1* or *Pdpn* (Figures S3C and S3D). We also identified clusters of BECs as positive for *Cd31*, *Cdh5*, or *Kdr* and negative for *Lyve1* and *Pdpn*, mesenchymal cells as *Pdgfra*⁺, and myofibroblasts as *Myh11*⁺ (Figures S3C and S3D). Within the *Pdgfra*⁺ mesenchymal populations, we identified telocytes as *Foxl1*⁺, *Pdgfra*^high and trophocytes as *Grem1*⁺, *Cd81*⁺, *Pdgfra*^low, among others (Figures S4F and S4G).

To compare the effect of 5FU treatment on crypt epithelial cells in control and knockout mice, we isolated *Epcam*⁺, *Cd44*⁺ cells from the merged cell population and re-performed cluster analysis (Figure 4C). We identified 9 clusters in *Epcam*⁺, *Cd44*⁺ epithelial cells: stem cells (*Olfm4*⁺, *Lgr5*⁺), cycling trTA cells (*Mki67*⁺), secretory progenitors (*Atoh1*⁺), secretory cells (including Paneth cells as *Lyz1*⁺ and goblet cells as *Muc2*⁺), enteroendocrine cells (*ChgA*⁺, *ChgB*⁺), and mature enterocytes (*Alpi*⁺) (Figures 4C and S3E). We also identified 3 other clusters of crypt epithelial cells. One was a *Sca1*^high (*Ly6a*) cluster;

Sca1 has been identified as a marker of dedifferentiation and of the transition to a fetal-like state in the small intestine after injury (Nusse et al., 2018). We also identified 2 clusters with elevated expression of markers such as *Cd74* and *Gpx2* (activated epithelium 1 and 2), which have been associated with activated epithelium in bacterial and parasitic infections (Haber et al., 2017) (Figures 4C and S3E). We determined differential cell composition and gene expression between control and knockout samples for each cluster. Knockout crypt epithelial cells had a lower expression of *Agr2*, *Ang4*, *Muc2*, *Ly6a* (*Sca1*), and *Il33*, among others (Figure 4D). Control crypt epithelial cells had a higher proportion of TA and *Sca1*^high cells (Figure S3F). Lower numbers of TA and *Sca1*^high cells in mutant mice than in control were accompanied by a higher proportion of *Olfm4*⁺, *Lgr5*⁺ cells compared with other crypt epithelial cells (Figure S3F). We confirmed decreased SCA-1 expression in knockout crypt epithelial cells compared to control cells via flow cytometry (Figures 4E–4G).

Loss of lymphatic *Rspo3* leads to a decrease in mucus-secreting cells

Secretory progenitors and secretory lineage cells were also decreased in knockout mice. Crypt epithelial cells displayed a decrease in genes involved in mucus production such as *Agr2* and *Muc2* (Figure 4D). *Agr2* is important for mucus secretion and processing, and its loss has been associated with mucus barrier dysfunction and colitis (Zheng et al., 2006). Using immunofluorescence, we confirmed a decrease in both MUC2 and AGR2 in crypt epithelial cells in mutant mice (Figures 4H–4L). Notably, these changes in secretory cells resulted in lower mucus levels in knockout mice compared to control mice after 5FU injury (Figure 4M).

Knockout LECs upregulate an endothelial-to-mesenchymal transition program after 5FU injury

We next asked what molecular changes occurred in LECs after 5FU injury in knockout mice compared to control mice. We isolated all ECs from the scRNA-seq data and performed clustering analysis. ECs grouped into 10 distinct clusters (Figures S4A and S4B). Among those, LECs were identified by the expression of *Lyve1* and included 2 clusters: clusters 0 and 3 (Figures S4A and S4B). In order to better understand these transcriptional changes in LECs, we performed differential expression analysis of all LECs in control versus knockout mice. Interestingly, genes related to the endothelial-to-mesenchymal transition, such as *Prss23* (Bayoumi et al., 2017), *Tgfb1* and *Tgfb2* (Maleszewska et al., 2013; Yoshimatsu et al., 2020), and genes shown to have anti-lymphangiogenic effects such as *Cavin1* (Yang et al., 2020), were expressed at significantly higher levels in *Rspo3*

(B) Gating strategy to isolate LECs and BECs. First, we selected CD45^Neg and EPCAM^Neg cells to exclude immune and epithelial cells, then isolated CD31⁺ endothelial cells, and finally distinguished LECs and BECs as PDPN⁺ and PDPN^Neg, respectively.

(C) UMAP (Uniform Manifold Approximation and Projection) plot of all ECs showing that LECs group in 2 clusters (cluster 0 and 10) and BECs group in 13 different clusters.

(D) UMAP plots of the expression of markers for pan-endothelial, lymphatic, and epithelial cells validating the identity of LECs and BECs.

(E) UMAP plots of *Lyve1*, *Rspo3*, *Wls*, and *Wnt2* expression inside EC clusters showing that LECs in the small intestine express high levels of *Rspo3*, *Wls*, and *Wnt2*.

(F) *Rspo3 in situ* hybridization (RNAscope) coupled with LYVE1 immunofluorescence of adult mouse small intestine demonstrating expression of *Rspo3* mRNA in LECs that are in proximity to the crypt region. Scale bar, 50 μm.

See also Figure S1.
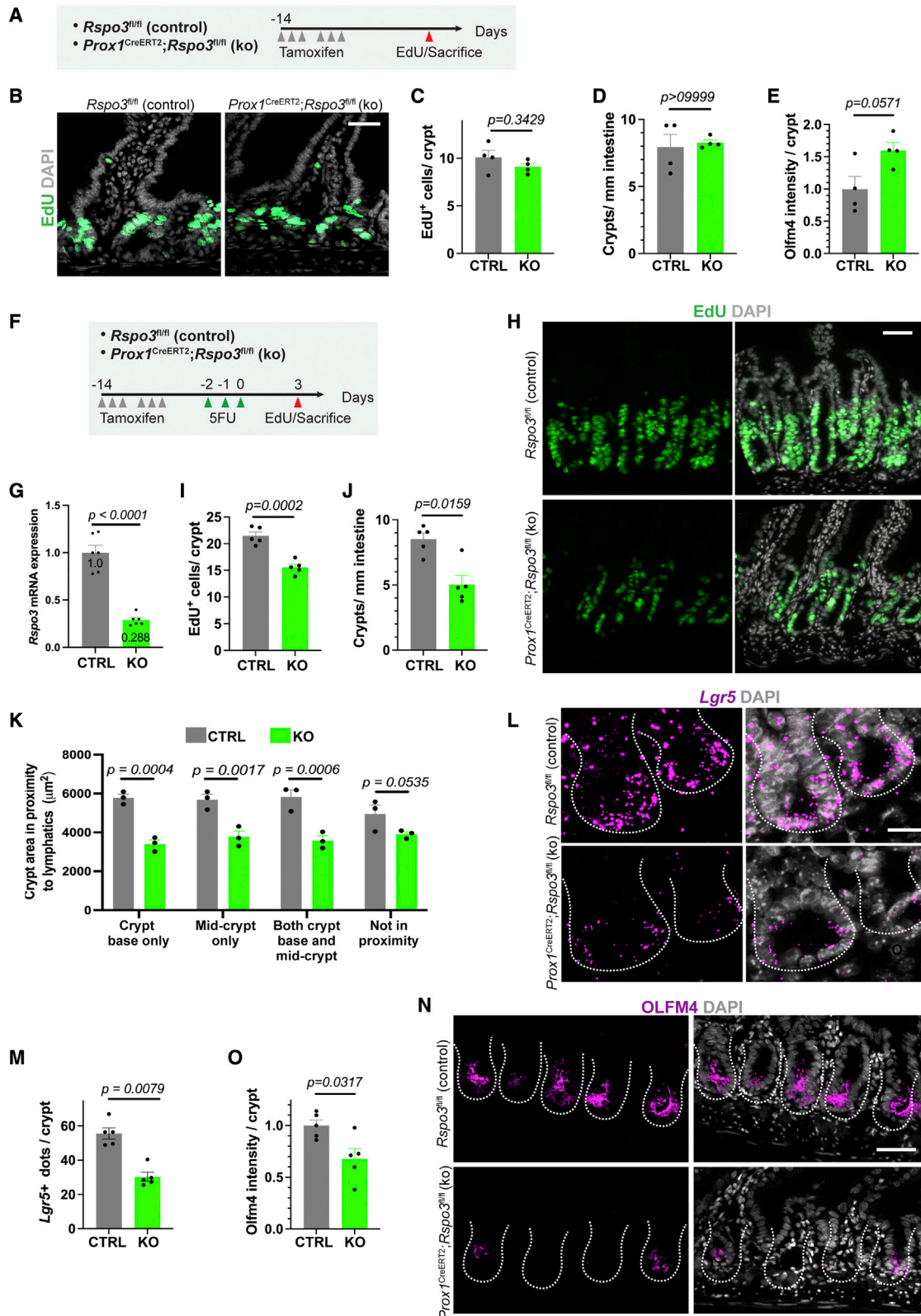
Figure 3. Lymphatic *Rspo3* is essential for intestinal recovery after 5FU injury

(A) Tamoxifen-induced *Prox1*[CreERT2];*Rspo3*^{fl/fl} knockout mice and control *Rspo3*^{fl/fl} were sacrificed 14 days after beginning of tamoxifen induction and after a 2-h EdU pulse.

knockout LECs (Figures S4C and S4D). Cluster 3, which consists largely of knockout LECs, was especially enriched in these genes. We confirmed these patterns of changes in LECs by performing qPCR analysis on FACS-isolated LECs (Figure S4E). Lastly, we examined the mesenchymal cell populations and observed that a new *Rspo3*^{neg} myofibroblast population was present in knockout mice, but not in control mice (Figure S4F and S4G).

In sum, loss of *Rspo3* from LECs leads to reduced crypt proliferation after cytotoxic injury, which is reflected in a lower number of TA and *Sca1*^{high} crypt epithelial cells. *Rspo3* loss in LECs also causes a decrease in mucus-secreting cells and a reduction in mucus production after 5FU injury.

DISCUSSION

The cellular components that constitute the ISC niche are currently the subject of intensive investigation, but the involvement of ECs has been understudied. We report that LECs are physically part of the niche, with large vessels located just under the crypts and in proximity to ISCs, and with smaller lacteal vessels ascending alongside the crypt to the top of villi. Together, more than 80% of crypts are in proximity to lymphatic vessels. Analysis of our scRNA-seq data revealed that LECs secrete several components of the Wnt pathway, such as *Rspo3*, *Wls*, and *Wnt2*. A parallel study utilizing spatial transcriptomics demonstrated that *Rspo3* and *Wnt2* are highly expressed in LECs in the crypt region, compared to lacteals in the villus region (Niec et al., 2022). By deleting *Rspo3* specifically in LECs, we demonstrated that LEC-secreted *Rspo3* is essential for the proper regeneration of the intestinal epithelium after injury caused by 5FU treatment. *Rspo3* knockout mice displayed a decrease in proliferative cells in the crypt and lower levels of SCA1+ cells after 5FU injury. Additionally, loss of *Rspo3* in LECs resulted in a marked decrease in mucus-producing cells and in levels of mucus after 5FU injury; this could potentially result in increased vulnerability of crypt epithelial cells to pathogens.

Rspo3 produced by LECs supports regeneration of the small intestine after 5FU-induced injury, but it is dispensable during homeostasis. This indicates that *Rspo3* is produced by several sources in the ISC niche during homeostasis. Consistent with this notion, other studies have shown that deletion of *Rspo3* in *Pdgfra*[+] fibroblasts (Goto et al., 2022; Greicius et al., 2018) or in myofibroblasts (Harnack et al., 2019) alone or generalized inhibition of RSPO3 by a neutralizing antibody (Storm et al., 2015) has no obvious effect on epithelial homeostasis. Additionally, loss of LEC-derived *Rspo3* seems to have a negligible effect on intestinal repair after ablation of *Lgr5*^{+} cells. We report that after a perturbation that is addressed through high levels of proliferation, such as 5FU treatment, *Rspo3* secreted by LECs is essential for the timely repair of epithelial cells. In addition, LECs themselves appear relatively structurally stable and are relatively unaffected by deleterious conditions, such as 5FU (this paper) or irradiation (Goto et al., 2022).

The 5FU injury triggers a massive proliferative and damage response, which is not seen when *Lgr5*^{+} cells alone are ablated. The number of proliferative cells per crypt stays about the same as during homeostasis after ablation of *Lgr5*^{+} cells, but it more than doubles after 5FU injury. The massive proliferation in the crypts after 5FU requires all sources of *Rspo3* available including that coming from LECs. We propose that there is a hierarchy of lymphatic *Rspo3* need that increases from homeostasis through ablation of *Lgr5*^{+} cells to 5FU injury. It therefore appears that intestinal maintenance and regeneration rely on distinct niche sources of *Rspo3*, presumably depending on the level of damage and the proliferation required to achieve repair. This also suggests that the intestinal niche should not be seen as static under all conditions but rather that different niche sources come together depending on need and injury to facilitate proper regeneration.

Angiocrine factors support stem cells and regenerative processes of several tissues. This has led to an appreciation that ECs are more than just the plumbing that carries blood and oxygen but rather that they provide essential molecular signaling for maintaining tissue function both *in vivo* and *in vitro* (Augustin and Koh, 2017)(Rafii et al., 2016)(Palikuqi et al., 2020). Our findings demonstrate that lymphangiocrine-derived factors in the intestine are critical for intestinal regeneration after cytotoxic injury. This suggests that LECs could be an important source of secreted factors in other tissues as well. The conclusion that LECs play a supportive role to ISCs and regenerative cells is also relevant to diseases in the gut. In colorectal cancer, lymphangiogenesis is one cause of the development of metastasis (Li et al., 2011; Tacconi et al., 2015). Our finding that, after 5FU treatment, LEC-secreted *Rspo3* contributes to ISC maintenance

(B) Representative images of EdU staining from control and knockout mice at homeostasis (n = 4 mice). Scale bar, 50 μm.

(C) Quantification of EdU^{+} cells per crypt at homeostasis for control (CTRL) and knockout (KO) mice (n = 4 mice).

(D) Quantification of total crypts per millimeter (mm) at homeostasis for control (CTRL) and knockout (KO) mice (n = 4 mice).

(E) Quantification of OLFM4 staining intensity for control (CTRL) and knockout (KO) mice at homeostasis (n = 4 mice).

(F) After tamoxifen induction, control (CTRL) and *Rspo3* knockout (KO) mice were treated for 3 days with 5FU at 75 mg/kg. Recovery was assessed at day 3 after injury. Mice were injected with EdU 2 h before sacrifice.

(G) Deletion efficiency as quantified by *Rspo3* mRNA levels analyzed by RT-qPCR in sorted LECs at day 3 after the end of 5FU treatment (n = 6 mice).

(H and I) Representative images of EdU staining in the crypts of control and *Rspo3* knockout mice at day 3 (H) and quantification of EdU^{+} cells per crypt at day 3 (n = 5 mice) (I). Scale bar, 50 μm.

(J) Quantification of total crypts per millimeter (mm) at day 3 after 5FU treatment for control (CTRL) and knockout (KO) mice (n = 5 mice).

(K) Quantification of crypt size (area in μm[2] of crypt section) in relation to their position to lymphatic vessels in control and *Rspo3* knockout mice at day 3 after 5FU treatment (n = 3 mice).

(L and M) Representative images of *Lgr5*^{+} *in situ* hybridization (RNAscope) for control and knockout mice at day 3 after 5FU (L) and quantification of *Lgr5* transcripts per crypt (n = 5 mice) (M). Scale bar, 20 μm.

(N) OLFM4 staining in control and knockout mice at day 3 after 5FU (n = 5 mice). Scale bar, 50 μm.

(O) Quantification of OLFM4 intensity staining per crypt at day 3 after 5FU (n = 5 mice). Bar graph data are mean ± SEM, Mann Whitney U test, two sided.

See also Figure S2.
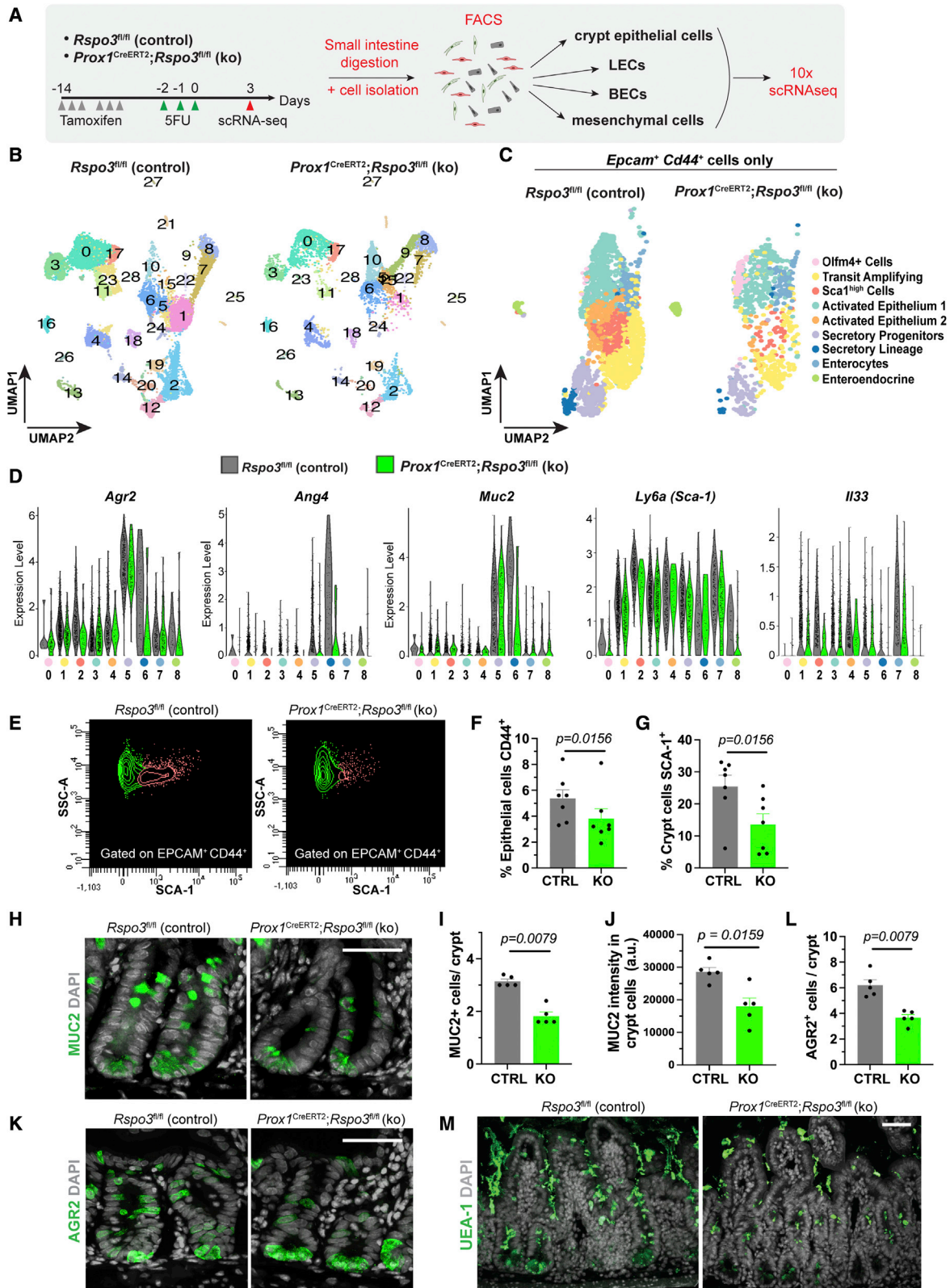
(legend on next page)

suggests that LECs could also be involved in the promotion of cancer. Furthermore, maintenance of the lymphatic vessel density of LECs after 5FU treatment raises questions about the potential involvement of LECs in cancer cell survival and escape from chemotherapy.

Limitations of the study

In our work, we determined that lymphatic-derived *Rspo3* contributes to intestinal regeneration after 5FU injury. However, we did not observe a phenotype after conditional deletion of *Rspo3* from the lymphatics during homeostasis. In a complementary study to ours, Goto et al. explored all sources of *Rspo3* in the intestine. They found that when *Rspo3* is deleted from both mesenchymal and lymphatic sources, ISC maintenance at homeostasis was significantly affected (Goto et al., 2022). We also concluded that LEC-derived *Rspo3* is dispensable for intestinal recovery after ablation of *Lgr5*^{+} cells, but it is possible that we could have identified a phenotype if we looked at shorter or longer time points after ablation of *Lgr5*^{+} cells.

STAR★METHODS

Detailed methods are provided in the online version of this paper and include the following:

- KEY RESOURCES TABLE
- RESOURCE AVAILABILITY
  - Lead contact
  - Materials availability
  - Data availability
- EXPERIMENTAL MODEL AND SUBJECT DETAILS
  - Mouse strains
- METHOD DETAILS
  - Tissue collection and preparation for microscopy
  - Immunofluorescence, RNAscope, EdU labeling on sections and whole mount staining
  - Quantification of staining
  - Tissue preparation and digestion
  - scRNAseq analysis
  - Mucin staining
  - mRNA extraction and RT-qPCR analysis
- QUANTIFICATION AND STATISTICAL ANALYSIS

REFERENCES

Abel, E., Ekman, T., Warnhammar, E., Hultborn, R., Jennische, E., and Lange, S. (2005). Early disturbance of microvascular function precedes chemotherapy-induced intestinal injury. Dig. Dis. Sci. *50*, 1729–1733. https://doi.org/10.1007/s10620-005-2926-9.

Aoki, R., Shoshkes-Carmel, M., Gao, N., Shin, S., May, C.L., Golson, M.L., Zahm, A.M., Ray, M., Wiser, C.L., Wright, C.V.E., and Kaestner, K.H. (2016). Foxl1-expressing mesenchymal cells constitute the intestinal stem cell niche. Cell. Mol. Gastroenterol. Hepatol. *2*, 175–188. https://doi.org/10.1016/j.jcmgh.2015.12.004.

Figure 4. Loss of LEC *Rspo3* results in decreased numbers of TA, SCA1^{high}, and mucus-secreting cells

(A) Schema of scRNA-seq experiment. Tamoxifen-treated control and knockout mice were administered 5FU on 3 consecutive days. Crypt epithelial cells, LECs, BECs, and other stromal cells were enriched by FACS, and the samples were submitted for 10X scRNA-seq analysis. Data are from 2 independent biological experiments. Each biological experiment included 2 control and 2 knockout mice.

(B) The sequenced cells group in 29 clusters as depicted in UMAP plots.

(C) Crypt epithelial cells were identified as *Epcam*[+], *Cd44*^{+} cells and re-clustered. Crypt epithelial cells group in 9 distinct clusters as shown in UMAP plots.

(D) Violin plot of differentially expressed genes (DEGs) in crypt epithelial cells from control (gray) versus knockout (green) mice.

(E) Flow cytometry analysis of SCA-1^{−} (green) and SCA-1^{+} (red) cells, gated on crypt epithelial cells (EPCAM^{+} and CD44^{+}), in control and knockout mice at day 3 after 5FU (n = 7 mice).

(F and G) Proportion of epithelial cells that are CD44^{+} (F) and crypt epithelial cells that are SCA-1^{+} (G) quantified by flow cytometry in control (CTRL) and *Rspo3* knockout (KO) mice at day 3 after 5FU (n = 7 mice).

(H–J) Representative images (H) and quantification (I) of MUC2^{+} cells and (J) quantification of MUC2 staining intensity in the crypts of control (CTRL) and *Rspo3* knockout (KO) mice at day 3 after 5FU (n = 5 mice).

(K and L) Representative images (K) and quantification (L) of AGR2^{+} cells in crypts of control (CTRL) and *Rspo3* knockout (KO) mice at day 3 after 5FU (n = 5 mice).

(M) Representative images of mucus (UEA-1) staining in control and *Rspo3* knockout mice at day 3 after 5FU (n = 4 mice). Bar graph data are mean ± SEM, Wilcoxon paired t test two sided (F and G) and Mann Whitney U test, two sided (I, J, and L).

See also Figures S3 and S4.

Augustin, H.G., and Koh, G.Y. (2017). Organotypic vasculature: From descriptive heterogeneity to functional pathophysiology. Science *357*, eaal2379. https://doi.org/10.1126/science.aal2379.

Barker, N., van Es, J.H., Kuipers, J., Kujala, P., van den Born, M., Cozijnsen, M., Haegebarth, A., Korving, J., Begthel, H., Peters, P.J., and Clevers, H. (2007). Identification of stem cells in small intestine and colon by marker gene Lgr5. Nature *449*, 1003–1007. https://doi.org/10.1038/nature06196.

Bayoumi, A.S., Teoh, J.P., Aonuma, T., Yuan, Z., Ruan, X., Tang, Y., Su, H., Weintraub, N.L., and Kim, I.M. (2017). MicroRNA-532 protects the heart in acute myocardial infarction, and represses prss23, a positive regulator of endothelial-to-mesenchymal transition. Cardiovasc. Res. *113*, 1603–1614. https://doi.org/10.1093/cvr/cvx132.

Bernier-Latmani, J., and Petrova, T.V. (2016). High-resolution 3D analysis of mouse small-intestinal stroma. Nature protocols *11*, 1617–1629. https://doi.org/10.1038/nprot.2016.092.

Bernier-Latmani, J., and Petrova, T.V. (2017). Intestinal lymphatic vasculature: Structure, mechanisms and functions. Nat. Rev. Gastroenterol. Hepatol. *14*, 510–526. https://doi.org/10.1038/nrgastro.2017.79.

Bernier-Latmani, J., Cisarovsky, C., Demir, C.S., Bruand, M., Jaquet, M., Davanture, S., Ragusa, S., Siegert, S., Dormond, O., Benedito, R., et al. (2015). DLL4 promotes continuous adult intestinal lacteal regeneration and dietary fat transport. J. Clin. Invest. *125*, 4572–4586. https://doi.org/10.1172/JCI82045.

Beumer, J., and Clevers, H. (2020). Cell fate specification and differentiation in the adult mammalian intestine. Nat. Rev. Mol. Cell Biol. *22*, 39–53. https://doi.org/10.1038/s41580-020-0278-0.

Butler, A., Hoffman, P., Smibert, P., Papalexi, E., and Satija, R. (2018). Integrating single-cell transcriptomic data across different conditions, technologies, and species. Nat. Biotechnol. *36*, 411–420. https://doi.org/10.1038/nbt.4096.

Butler, J.M., Nolan, D.J., Vertes, E.L., Varnum-Finney, B., Kobayashi, H., Hooper, A.T., Seandel, M., Shido, K., White, I.A., Kobayashi, M., et al. (2010). Endothelial cells are essential for the self-renewal and repopulation of Notch-dependent hematopoietic stem cells. Cell Stem Cell *6*, 251–264. https://doi.org/10.1016/j.stem.2010.02.001.

Cifarelli, V., and Eichmann, A. (2019). The intestinal lymphatic system: functions and metabolic implications. Cell. Mol. Gastroenterol. Hepatol. *7*, 503–513. https://doi.org/10.1016/j.jcmgh.2018.12.002.

de Lau, W., Barker, N., Low, T.Y., Koo, B.-K., Li, V.S.W., Teunissen, H., Kujala, P., Haegebarth, A., Peters, P.J., van de Wetering, M., et al. (2011). Lgr5 homologues associate with Wnt receptors and mediate R-spondin signalling. Nature *476*, 293–297. https://doi.org/10.1038/nature10337.

Degirmenci, B., Valenta, T., Dimitrieva, S., Hausmann, G., and Basler, K. (2018). GLI1-expressing mesenchymal cells form the essential Wnt-secreting niche for colon stem cells. Nature *558*, 449–453. https://doi.org/10.1038/s41586-018-0190-3.

Ding, B.S., Nolan, D.J., Butler, J.M., James, D., Babazadeh, A.O., Rosenwaks, Z., Mittal, V., Kobayashi, H., Shido, K., Lyden, D., et al. (2010). Inductive angiocrine signals from sinusoidal endothelium are required for liver regeneration. Nature *468*, 310–315. https://doi.org/10.1038/nature09493.

Ding, B.S., Nolan, D.J., Guo, P., Babazadeh, A.O., Cao, Z., Rosenwaks, Z., Crystal, R.G., Simons, M., Sato, T.N., Worgall, S., et al. (2011). Endothelial-derived angiocrine signals induce and sustain regenerative lung alveolarization. Cell *147*, 539–553. https://doi.org/10.1016/j.cell.2011.10.003.

Ding, L., Saunders, T.L., Enikolopov, G., and Morrison, S.J. (2012). Endothelial and perivascular cells maintain haematopoietic stem cells. Nature *481*, 457–462. https://doi.org/10.1038/nature10783.

Gehart, H., and Clevers, H. (2019). Tales from the crypt: New insights into intestinal stem cells. Nat. Rev. Gastroenterol. Hepatol. *16*, 19–34. https://doi.org/10.1038/s41575-018-0081-y.

Glinka, A., Dolde, C., Kirsch, N., Huang, Y.L., Kazanskaya, O., Ingelfinger, D., Boutros, M., Cruciat, C.M., and Niehrs, C. (2011). LGR4 and LGR5 are R-spondin receptors mediating Wnt/β-catenin and Wnt/PCP signalling. EMBO Rep. *12*, 1055–1061. https://doi.org/10.1038/embor.2011.175.

Goto, N., Imada, S., Deshpande, V., and Yilmaz, Ö.H. (2022). Lymphatics constitute a novel component of the intestinal stem cell niche. Cell Stem Cell *29*. Published online August 4, 2022. https://doi.org/10.1016/j.stem.2022.06.013.

Greicius, G., Kabiri, Z., Sigmundsson, K., Liang, C., Bunte, R., Singh, M.K., and Virshup, D.M. (2018). pericryptal stromal cells are the critical source of Wnts and RSPO3 for murine intestinal stem cells in vivo. Proc. Natl. Acad. Sci. USA. *115*, E3173–E3181. https://doi.org/10.1073/pnas.1713510115.

Gur-Cohen, S., Yang, H., Baksh, S.C., Miao, Y., Levorse, J., Kataru, R.P., Liu, X., Cruz-Racelis, J.d.l., Mehrara, B.J., and Fuchs, E. (2019). Stem cell-driven lymphatic remodeling coordinates tissue regeneration. Science *366*, 1218–1225. https://doi.org/10.1126/science.aay4509.

Haber, A.L., Biton, M., Rogel, N., Herbst, R.H., Shekhar, K., Smillie, C., Burgin, G., Delorey, T.M., Howitt, M.R., Katz, Y., et al. (2017). A single-cell survey of the small intestinal epithelium. Nature *551*, 333–339. https://doi.org/10.1038/nature24489.

Hao, H.-X., Xie, Y., Zhang, Y., Charlat, O., Oster, E., Avello, M., Lei, H., Mickanin, C., Liu, D., Ruffner, H., et al. (2012). ZNRF3 promotes Wnt receptor turnover in an R-spondin-sensitive manner. Nature *485*, 195–200. https://doi.org/10.1038/nature11019.

Harnack, C., Berger, H., Antanaviciute, A., Vidal, R., Sauer, S., Simmons, A., Meyer, T.F., and Sigal, M. (2019). R-spondin 3 promotes stem cell recovery and epithelial regeneration in the colon. Nat. Commun. *10*, 4368. https://doi.org/10.1038/s41467-019-12349-5.

Hu, J., Srivastava, K., Wieland, M., Runge, A., Mogler, C., Besemfelder, E., Terhardt, D., Vogel, M.J., Cao, L., Korn, C., et al. (2014). Endothelial cell-derived angiopoietin-2 controls liver regeneration as a spatiotemporal rheostat. Science *343*, 416–419. https://doi.org/10.1126/science.1244880.

Kabiri, Z. (2014). Stroma provides an intestinal stem cell niche in the absence of epithelial Wnts. Development *141*, 2206–2215. https://doi.org/10.1242/dev.104976.

Kalucka, J., de Rooij, L.P.M.H., Goveia, J., Rohlenova, K., Dumas, S.J., Meta, E., Conchinha, N.V., Taverna, F., Teuwen, L.A., Veys, K., et al. (2020). Single-Cell transcriptome atlas of murine endothelial cells. Cell *180*, 764–779.e20. https://doi.org/10.1016/j.cell.2020.01.015.

Kinchen, J., Chen, H.H., Parikh, K., Antanaviciute, A., Jagielowicz, M., Fawkner-Corbett, D., Ashley, N., Cubitt, L., Mellado-Gomez, E., Attar, M., et al. (2018). Structural remodeling of the human colonic mesenchyme in inflammatory bowel disease. Cell *175*, 372–386.e17. https://doi.org/10.1016/j.cell.2018.08.067.

Kondo, A., and Kaestner, K.H. (2019). Emerging diverse roles of telocytes. Development *146*, dev175018. https://doi.org/10.1242/dev.175018.

Li, X., Liu, B., Xiao, J., Yuan, Y., Ma, J., and Zhang, Y. (2011). Roles of VEGF-C and Smad4 in the lymphangiogenesis, lymphatic metastasis, and prognosis in colon cancer. J. Gastrointest. Surg. *15*, 2001–2010. https://doi.org/10.1007/s11605-011-1627-2.

Liao, Y., Wang, J., Jaehnig, E.J., Shi, Z., and Zhang, B. (2019). WebGestalt 2019: Gene set analysis toolkit with revamped UIs and APIs. Nucleic Acids Res. *47*, W199–W205. https://doi.org/10.1093/nar/gkz401.

Liu, X., De la Cruz, E., Gu, X., Balint, L., Oxendine-Burns, M., Terrones, T., Ma, W., Kuo, H.-H., Lantz, C., Bansal, T., et al. (2020). Lymphoangiocrine signals promote cardiac growth and repair. Nature *588*, 705–711. https://doi.org/10.1038/s41586-020-2998-x.

Maleszewska, M., Moonen, J.R.A.J., Huijkman, N., van de Sluis, B., Krenning, G., and Harmsen, M.C. (2013). IL-1β and TGFβ2 synergistically induce endothelial to mesenchymal transition in an NFκB-dependent manner. Immunobiology *218*, 443–454. https://doi.org/10.1016/j.imbio.2012.05.026.

Matsumoto, K., Mitani, T.T., Horiguchi, S.A., Kaneshiro, J., Murakami, T.C., Mano, T., Fujishima, H., Konno, A., Watanabe, T.M., Hirai, H., and Ueda, H.R. (2019). Advanced CUBIC tissue clearing for whole-organ cell profiling. Nat. Protoc. *14*, 3506–3537. https://doi.org/10.1038/s41596-019-0240-9.

McCarthy, N., Kraiczy, J., and Shivdasani, R.A. (2020a). Cellular and molecular architecture of the intestinal stem cell niche. Nat. Cell Biol. *22*, 1033–1041. https://doi.org/10.1038/s41556-020-0567-z.

McCarthy, N., Manieri, E., Storm, E.E., Saadatpour, A., Luoma, A.M., Kapoor, V.N., Madha, S., Gaynor, L.T., Cox, C., Keerthivasan, S., et al. (2020b). Distinct mesenchymal cell populations generate the essential intestinal BMP signaling gradient. Cell Stem Cell 26, 391–402.e5. https://doi.org/10.1016/j.stem.2020.01.008.

Niec, R.E., Chu, T., Schernthanner, M., Gur-Cohen, S., Hidalgo, L., Pasolli, H.A., Luckett, K.A., Wang, Z., Bhalla, S.R., Cambuli, F., et al. (2022). Lymphatics act as a signaling hub to regulate intestinal stem cell activity. Cell Stem Cell 29, 1067–1082. https://doi.org/10.1016/j.stem.2022.05.007.

Nusse, Y.M., Savage, A.K., Marangoni, P., Rosendahl-Huber, A.K.M., Landman, T.A., de Sauvage, F.J., Locksley, R.M., and Klein, O.D. (2018). Parasitic helminths induce fetal-like reversion in the intestinal stem cell niche. Nature 559, 109–113. https://doi.org/10.1038/s41586-018-0257-1.

Ogasawara, R., Hashimoto, D., Kimura, S., Hayase, E., Ara, T., Takahashi, S., Ohigashi, H., Yoshioka, K., Tateno, T., Yokoyama, E., et al. (2018). Intestinal lymphatic endothelial cells produce R-Spondin3. Sci. Rep. 8, 10719. https://doi.org/10.1038/s41598-018-29100-7.

Palikuqi, B., Nguyen, D.T., Li, G., Schreiner, R., Pellegata, A.F., Liu, Y., Redmond, D., Geng, F., Lin, Y., Gómez-Salinero, J.M., et al. (2020). Adaptable haemodynamic endothelial cells for organogenesis and tumorigenesis. Nature 585, 426–432. https://doi.org/10.1038/s41586-020-2712-z.

Palikuqi, B., Rispal, J., and Klein, O. (2021). Good neighbors: The niche that fine tunes mammalian intestinal regeneration. Cold Spring Harb. Perspect. Biol.a040865 https://doi.org/10.1101/cshperspect.a040865.

Paris, F., Fuks, Z., Kang, A., Capodieci, P., Juan, G., Ehleiter, D., Haimovitz-Friedman, A., Cordon-Cardo, C., and Kolesnick, R. (2001). Endothelial apoptosis as the primary lesion initiating intestinal radiation damage in mice. Science 293, 293–297. https://doi.org/10.1126/science.1060191.

Rafii, S., Butler, J.M., and Ding, B.S. (2016). Angiocrine functions of organ-specific endothelial cells. Nature 529, 316–325. https://doi.org/10.1038/nature17040.

Rehal, S., Stephens, M., Roizes, S., Liao, S., and von der Weid, P.Y. (2018). Acute small intestinal inflammation results in persistent lymphatic alterations. Am. J. Physiol. Gastrointest. Liver Physiol. 314, G408–G417. https://doi.org/10.1152/ajpgi.00340.2017.

Sato, T., Vries, R.G., Snippert, H.J., van de Wetering, M., Barker, N., Stange, D.E., van Es, J.H., Abo, A., Kujala, P., Peters, P.J., and Clevers, H. (2009). Single Lgr5 stem cells build crypt-villus structures in vitro without a mesenchymal niche. Nature 459, 262–265. https://doi.org/10.1038/nature07935.

Scholz, B., Korn, C., Wojtarowicz, J., Mogler, C., Augustin, I., Boutros, M., Niehrs, C., and Augustin, H.G. (2016). Endothelial RSPO3 controls vascular stability and pruning through non-canonical WNT/Ca(2+)/NFAT signaling. Dev. Cell 36, 79–93. https://doi.org/10.1016/j.devcel.2015.12.015.

Shoshkes-Carmel, M., Wang, Y.J., Wangensteen, K.J., Tóth, B., Kondo, A., Massasa, E.E., Itzkovitz, S., and Kaestner, K.H. (2018). Subepithelial telocytes are an important source of Wnts that supports intestinal crypts. Nature 557, 242–246. https://doi.org/10.1038/s41586-018-0084-4.

Storm, E.E., Durinck, S., de Sousa e Melo, F., Tremayne, J., Kljavin, N., Tan, C., Ye, X., Chiu, C., Pham, T., Hongo, J.-A., et al. (2015). Targeting PTPRK-RSPO3 colon tumours promotes differentiation and loss of stem-cell function. Nature 529, 97–100. https://doi.org/10.1038/nature16466.

Stzepourginski, I., Nigro, G., Jacob, J.M., Dulauroy, S., Sansonetti, P.J., Eberl, G., and Peduto, L. (2017). CD34+ mesenchymal cells are a major component of the intestinal stem cells niche at homeostasis and after injury. Proc. Natl. Acad. Sci. USA. 114, E506–E513. https://doi.org/10.1073/pnas.1620059114.

Tacconi, C., Correale, C., Gandelli, A., Spinelli, A., Dejana, E., D'Alessio, S., and Danese, S. (2015). Vascular endothelial growth factor C disrupts the endothelial lymphatic barrier to promote colorectal cancer invasion. Gastroenterology 148, 1438–1451.e8. https://doi.org/10.1053/j.gastro.2015.03.005.

Tian, H., Biehs, B., Warming, S., Leong, K.G., Rangell, L., Klein, O.D., and de Sauvage, F.J. (2011). A reserve stem cell population in small intestine renders Lgr5-positive cells dispensable. Nature 478, 255–259. https://doi.org/10.1038/nature10408.

Valenta, T., Degirmenci, B., Moor, A.E., Herr, P., Zimmerli, D., Moor, M.B., Hausmann, G., Cantù, C., Aguet, M., and Basler, K. (2016). Wnt ligands secreted by subepithelial mesenchymal cells are essential for the survival of intestinal stem cells and gut homeostasis. Cell Rep. 15, 911–918. https://doi.org/10.1016/j.celrep.2016.03.088.

Wertheimer, T., Velardi, E., Tsai, J., Cooper, K., Xiao, S., Kloss, C.C., Ottmüller, K.J., Mokhtari, Z., Brede, C., deRoos, P., et al. (2018). Production of BMP4 by endothelial cells is crucial for endogenous thymic regeneration. Sci. Immunol. 3, eaal2736. https://doi.org/10.1126/sciimmunol.aal2736.

Yan, K.S., Janda, C.Y., Chang, J., Zheng, G.X.Y., Larkin, K.A., Luca, V.C., Chia, L.A., Mah, A.T., Han, A., Terry, J.M., et al. (2017). Non-equivalence of Wnt and R-spondin ligands during Lgr5. Nature 545, 238–242. https://doi.org/10.1038/nature22313.

Yang, X., Kim, J.-d., Gu, Q., Yan, Q., Astin, J., Crosier, P.S., Yu, P., Rockson, S.G., and Fang, L. (2020). AIBP-CAV1-VEGFR3 axis Dictates Lymphatic Cell Fate and Controls Lymphangiogenesis. https://doi.org/10.1101/2020.10.16.342998.

Yoshimatsu, Y., Kimuro, S., Pauty, J., Takagaki, K., Nomiyama, S., Inagawa, A., Maeda, K., Podyma-Inoue, K.A., Kajiya, K., Matsunaga, Y.T., and Watabe, T. (2020). TGF-beta and TNF-alpha cooperatively induce mesenchymal transition of lymphatic endothelial cells via activation of Activin signals. PLoS One 15, e0232356. https://doi.org/10.1371/journal.pone.0232356.

Zheng, W., Rosenstiel, P., Huse, K., Sina, C., Valentonyte, R., Mah, N., Zeitlmann, L., Grosse, J., Ruf, N., Nürnberg, P., et al. (2006). Evaluation of AGR2 and AGR3 as candidate genes for inflammatory bowel disease. Genes Immun. 7, 11–18. https://doi.org/10.1038/sj.gene.6364263.

STAR★METHODS

KEY RESOURCES TABLE

REAGENT or RESOURCE	SOURCE	IDENTIFIER
Antibodies		
Rat monoclonal anti-LYVE1 (clone ALY7)	eBioscience	Cat# 14-0443-82; RRID:AB_1633414
Rabbit polyclonal anti-LYVE1	AngioBio	Cat# 11-034; RRID:AB_2813732
Goat polyclonal anti-PDGFRA	R&D systems	Cat# AF1062; RRID:AB_2236897
Rabbit monoclonal anti-OLFM4 (clone D6Y5A)	Cell signaling technology	Cat# 39141; RRID:AB_2650511
Rabbit polyclonal anti-MUC2	Novus biologicals	Cat# NBP1-31231; RRID:AB_10003763
Rabbit polyclonal anti-AGR2	Origene	Cat# TA336715
Donkey anti-Goat IgG Secondary Antibody (Alexa Fluor Plus 488)	Thermo Fischer Scientific	Cat# A32814; RRID:AB_2762838
Donkey Anti-Rat IgG Secondary Antibody (Alexa Fluor 647)	Jackson ImmunoResearch Labs	Cat# 712-605-153; RRID:AB_2340694
Donkey Anti-Rat IgG Secondary Antibody (Alexa Fluor 488)	Thermo Fischer Scientific	Cat# A-21208; RRID:AB_2535794
Donkey anti-Goat IgG Secondary Antibody (Alexa Fluor Plus 647)	Thermo Fischer Scientific	Cat# A32849; RRID:AB_2762840
Donkey Anti-Rabbit IgG Secondary Antibody (Alexa Fluor 555)	Thermo Fischer Scientific	Cat# A32794; RRID:AB_2762834
Goat Anti-Rabbit IgG Secondary Antibody (Alexa Fluor 488)	Thermo Fischer Scientific	Cat# A-11008; RRID:AB_143165
Goat Anti-Rabbit IgG Secondary Antibody (Alexa Fluor 568)	Invitrogen	Cat# A-11011; RRID:AB_143157
Alexa Fluor 647 anti-mouse CD326 (Ep-CAM) antibody	BioLegend	Cat# 118212; RRID:AB_1134101
Alexa Fluor 488 anti-mouse CD31 antibody	BioLegend	Cat# 102414; RRID:AB_493408
APC anti-mouse CD326 (Ep-CAM) antibody	BioLegend	Cat# 118214; RRID:AB_1134102
PE/Cyanine7 anti-mouse Podoplanin antibody	BioLegend	Cat# 127412; RRID:AB_10613648
PE-Cyanine7 anti-mouse LYVE1 Monoclonal Antibody (ALY7)	Thermo Fisher Scientific	Cat# 25-0443-82; RRID:AB_2802237
PE/Cyanine7 anti-mouse/human CD44 antibody	BioLegend	Cat# 103030; RRID:AB_830787
Brilliant Violet 421 anti-mouse CD45 antibody	BioLegend	Cat# 103134; RRID:AB_2562559
PE anti-mouse CD45 antibody	BioLegend	Cat# 103106; RRID:AB_312971
Alexa Fluor 647 anti-mouse CD144 (VE-cadherin) antibody	BioLegend	Cat# 138006; RRID:AB_10569114
APC anti-mouse Ly-6A/E (Sca-1) Monoclonal Antibody (D7)	eBioscience	Cat# 17-5981-82; RRID:AB_469487
Chemicals, peptides, and recombinant proteins		
ProLong Gold Antifade Mounting Solution	Thermo Fischer Scientific	Cat# P36930
Tamoxifen	Sigma-Aldrich	Cat# T5648-5G
Corn Oil	Sigma-Aldrich	Cat# C8267
Macs SmartStrainers	Miltenyi Biotec	Cat# 130-110-916
Triton X-100	Sigma-Aldrich	Cat# T8787
Normal Donkey Serum	Jackson ImmunoResearch	Cat# 017-000-121
Animal-free Blocker	Vector Laboratories	Cat# sp-5030
PFA	Fischer Scientific	Cat# 04042
Sucrose	VWR	Cat# JT4072-7
Tissue-Tek O.C.T. Compound	Sakuraus	Cat# 4583
N-butyldiethanolamine	TCI Chemicals	Cat# TCI-B0725
Antigen Unmasking Solution, Citrate-Based	VWR	Cat# 101098-054

(Continued on next page)

Continued

REAGENT or RESOURCE	SOURCE	IDENTIFIER
DAPI	Sigma-Aldrich	Cat# D9564
RPMI-1640 Medium	Sigma-Aldrich	Cat# R7509
Glutamax	Thermo Fisher Scientific	Cat# 35050061
MEM Non Essential Amino Acids Solution (100X)	Thermo Scientific	Cat# 11140050
HEPES	Thermo Fisher Scientific	Cat# 15630080
Penicillin Streptomycin	Thermo Fisher Scientific	Cat# 15140122
EDTA	Sigma-Aldrich	Cat# E5134
DTT	Sigma-Aldrich	Cat# 10197777001
HBSS	Thermo Scientific	Cat# 14175095
Collagenase A	Sigma-Aldrich	Cat# 10103586001
Dispase II	Sigma-Aldrich	Cat# 4942078001
DNAse	Worthington Biochemical	Cat# LS002007
iTaq™ Universal SYBR® Green Supermix	Biorad	Cat# 1725124
Lectin from *Ulex europaeus* (FITC conjugated)	Sigma-Aldrich	Cat# L9006
Critical commercial assays		
RNAscope Multiplex Fluorescent V2 Assay	ACD	Cat# 323100
Click-iT™ Plus EdU Alexa Fluor™ 647 Imaging Kit	Thermo Fisher Scientific	Cat# C10640
PicoPure™ RNA Isolation Kit	Thermo Scientific	Cat# KIT0204
High-Capacity cDNA Reverse Transcription Kit	Thermo Scientific	Cat# 4368814
Deposited data		
All scRNAseq data has been deposited on GEO	This paper	GEO: GSE198469
Experimental models: Organisms/strains		
Mouse strain: *Rspo3$^{fl/fl}$*		Christof Niehrs (Institute of Molecular Biology)
Mouse strain: *Prox1^{CreERT2}*	The Jackson Laboratory	JAX: 022075
Mouse strain: *Lgr5$^{DTR/GFP}$*	Genentech (Dr. Frederic de Sauvage)	N/A
Mouse strain: *Lgr5$^{GFP-IRES-CreERT2}$*	The Jackson Laboratory	JAX: 008875
Oligonucleotides		
RNAscope Probe- Mm-Lgr5	ACD	Cat# 312171
RNAscope Probe- Mm-Rspo3	ACD	Cat# 402011
Rspo3 primers Fw: GACTCGCCTAACACCTACATAC RV GACATTAGGATGCATTCTTCGC	This paper	N/A
Apoa1 primers Fw: CGCTAATGTGTATGTGGATGCG Rv: CCCAATCTGTTTCTTTCTCCAGG	This paper	N/A
Cavin1 primers Fw: CCAGATCCAGCTGACCCAAG Rv: TTCTTTATCTGGCCGGCCTG	This paper	N/A
Prss23 primers Fw: CCGCACAGAGACTCGGGT Rv: CCAGTGCAGCCAGTAGACAA	This paper	N/A
Tgfb1 primers Fw: TACAACAGCACCCGCGAC Rv: ACAGCAATGGGGGGTTCGG	This paper	N/A
Tgfb2 primers Fw: AGGGATCTTGGATGGAAATGGA Rv: CCAATGTAATAGAGAATGGTCAGTGG	This paper	N/A
Vim primers Fw: CGTTTCCAAGCCTGACCTCA Rv: GGCATCCACTTCACAGGTGA	This paper	N/A
Software and algorithms		
GraphPad Prism 9		https://www.graphpad.com
ImageJ (Fiji)	https://imagej.net/software/fiji/	v2.1.0/1.53c; RRID:SCR_002285
Adobe Illustrator	https://www.adobe.com	v25.4
R	https://www.r-project.org/	v.4.0.3
BD FACS Diva	https://www.bdbiosciences.com/	v.8.0.1

Continued

REAGENT or RESOURCE	SOURCE	IDENTIFIER
ZenBlue	https://www.zeiss.com/	v.3.1
WEB-GESTALT (WEB-based GEne SeT AnaLysis Toolkit)	https://www.webgestalt.org/	N/A
Seurat		v.4.1.0
Cell Ranger	https://10xgenomics.com	v.5.0.1
Biorender	https://biorender.com	N/A

RESOURCE AVAILABILITY

Lead contact

Further information and requests for resources and reagents should be directed to and will be fulfilled by the lead contact, Ophir Klein (Ophir.klein@ucsf.edu).

Materials availability

All the materials will be available upon request to the lead contact under material transfer agreement with UCSF.

Data availability

All scRNAseq data have been deposited on the Gene Expression Omnibus (GEO) and can be viewed under accession number GSE198469. This manuscript did not generate any new code. Any additional information required to reanalyze the data reported in this work is available from the lead contact upon request.

EXPERIMENTAL MODEL AND SUBJECT DETAILS

Mouse strains

All mouse experiments were conducted under the IACUC protocol AN176864 at the University of California San Francisco. All mice (male and female) were used at 8-12 weeks of age at the beginning of each experiment. *Rspo3*$^{fl/fl}$ mice were a gift of Christof Niehrs (Scholz et al., 2016), *Prox1*^{CreERT2} mice were purchased from Jackson labs (022,075), *Lgr5*$^{DTR/GFP}$ were originally derived at Genentech and are a kind gift of Fred de Sauvage (Tian et al., 2011), *Lgr5*$^{GFP-IRES-CreERT2}$ were purchased from Jackson labs (008875; (Barker et al., 2007)). For knock-out induction, mice were gavaged with tamoxifen in corn oil (200 mg/kg) 6 times, 2 × 3 days interspersed by 3 days of rest. For EdU proliferation experiments, mice were injected with EdU (5 mg/mL) 2 h before sacrifice. For injury experiments, mice were injected for 3 consecutive days with either 5FU at 75 mg/kg in 0.9% saline or Diphtheria toxin (DT) (50 μg/kg). For vessel visualization, mice were injected with an antibody against VECAD (25 μg/mouse in 100 μL of PBS) conjugated to Alexa-647 8 min prior to sacrifice.

METHOD DETAILS

Tissue collection and preparation for microscopy

For all microscopy experiments, the jejunum was collected and fixed in 4% PFA for 24 h. For sections, tissues were incubated in 30% sucrose for 24 h at 4°C and then embedded in OCT before being sectioned to a thickness of 8 μm. For whole mount, fixed tissues were cleared for 3 to 6 days in CUBIC-L solution (10% N-butyldiethanolamine, 10% Triton X-100 (Matsumoto et al., 2019).

Immunofluorescence, RNAscope, EdU labeling on sections and whole mount staining

Frozen sections were baked at 60°C for 30 min, unmasked for 30 min, blocked (5% NDS, 1X Animal Free blocking, 0.3% Triton X-100) for 1 h and incubated overnight with primary antibodies at 4°C (table). Then, sections were incubated with secondary antibodies for 1 h at RT (table).

RNAscope was done according to the manufacturer's protocol. Briefly, the sections were post-fixed in 4% PFA, incubated with hydrogen peroxide to inhibit endogenous peroxidase before performing target retrieval. Subsequently, the tissues were incubated with specific RNA probes (table), followed by revelation and amplification steps.

For EdU labeling, after the baking, slides were permeabilized for 5 min in 1% Triton X-100 and EdU staining performed according to manufacturer protocol (table).

For whole mount staining, 1 cm tissue pieces were blocked for 1 day, incubated with primary and then secondary antibodies for 2 days and finally post-fixed for 1 day in 4% PFA (Bernier-Latmani and Petrova, 2016). Each step was done at 4°C.

For all staining and labeling, tissues were counterstained with DAPI and mounted in Prolong Gold. The images were taken using a Zeiss 900 with Airyscan system.

Quantification of staining

All image quantifications were done using ImageJ software. The proliferative cell number was quantified by counting the number of EdU$^+$ cells per crypt and calculating the mean for each mouse (~30 crypts per mouse). MUC2$^+$ and AGR2$^+$ cell numbers were quantified by counting positive cells in the crypts except Paneth cells present at the bottom (~30 crypts per mouse). For quantification of MUC2 intensity, crypts were traced and manually segmented. Yen thresholding followed by particle analysis was then performed on the segmented image and the mean grey value was measured for each region of interest (~40 crypts/mouse). The crypt number was calculated by counting OLFM4$^+$ crypts in 20 to 30 mm of tissue length. The OLFM4 intensity was analyzed by calculating the mean of the staining in a defined area corresponding to the crypt (~50 crypts per mouse). *Lgr5* RNAscope was quantified by calculating the mean of positive dots in each crypt (~20 crypts per mouse). For the quantification of crypt number in close proximity to lymphatic vessels, crypts were assigned to different categories: 1) crypt base: at least one cell of the crypt base is above a lymphatic vessel, 2) mid-crypt: at least one side of the mid-crypt is beside of a lymphatic vessel, 3) mid-crypt only, 4) crypt base only, 5) both crypt base and mid-crypt, 6) either crypt base or mid-crypt and 7) not in proximity: neither crypt-base nor mid-crypt (~200 crypts per mouse). For the quantification of lymphatic vessel density, after Z-projection of all optical sections, the area fraction of the LYVE-1 signal (LYVE-1 positive area on total area) was quantified for each mouse. For crypt size calculation, in whole mount staining, crypts were first classified as in proximity or not with lymphatics as previously, then transverse optical sections at the mid crypt position were chosen to quantify the area of the width using ImageJ (~200 crypts per mouse).

Tissue preparation and digestion

Small intestines from adult mice were collected and cut into small pieces (0.5 cm) and put in 30 mL of dissociation solution (RPMI + 1% Glutamax, 1% non-essential amino acids, 2.5% HEPES, 1% Pen-strep, 5 mM EDTA, 3% FBS and 1 μM DTT) in a rotator at 37°C for 30 min. Tissues were washed twice in HBSS, spun down and further minced using scissors. The minced tissue was then digested in a rotator for 30 min at 37°C in 4 mL of digestion solution (Collagenase A (2.5 mg/mL), Dispase II (1 U/ml) and DNAse (30 μg/mL) in HBSS with 1% Glutamax, 1% non-essential amino acids and 2.5% HEPES). The cells were strained (100 μM strainer) and the leftover tissue digested for another 30 min in more 4 mL of digestion solution. Both fractions were stained with antibodies and Aria II with a 100-micron nozzle utilized to perform the sort.

For sequencing experiments during homeostasis

Small intestines were digested and prepared as described above. Data are from two biological replicates. Each biological replicates contains cells from one adult male and one adult female mouse. Lymphatic endothelial cells were sorted as CD31$^+$, PDPN$^+$, EPCAM^{neg}, CD45^{neg} and blood endothelial cells as CD31$^+$, PDPN^{neg}, EPCAM^{neg} and CD45^{neg}. 6000 BECs and 2000 LECs were sequenced in total.

For 5FU experiments

At day 3 after the last 5FU injection, small intestines were digested and prepared as described above. Data are from two biological replicates. Each biological replicate contains cells from one adult male and one adult female mouse. Crypt epithelial cells were sorted as EPCAM$^+$, CD44$^+$, CD45^{neg}, CD31^{neg}, lymphatic endothelial cells were sorted as CD31$^+$, PDPN$^+$, EPCAM^{neg}, CD45^{neg}, blood endothelial cells as CD31$^+$, PDPN^{neg}, EPCAM^{neg}, CD45^{neg}, epithelial cells as EPCAM$^+$, CD45^{neg}, CD31^{neg} and stroma cells EPCAM^{neg}, CD45^{neg}, CD31^{neg}. After sorting, the different populations were mixed and loaded into 10x Chromium.

For SCA-1 validation experiments

At day 3 after the last 5FU injection, small intestines were digested and prepared as described above. Data are from 7 biological replicates. SCA-1$^+$ cells were gated on the EPCAM$^+$, CD44$^+$, CD45^{neg}, CD31^{neg} population.

scRNAseq analysis

The single-cell suspension was loaded onto the 10X Chromium Single Cell instrument (10X Genomics). Single-cell barcoding, and cDNA libraries were constructed using the 10X Chromium single-cell 3' Library Kit according to the manufacturer's protocol. Libraries were sequenced on an Illumina NovaSeq 6000 and the sequence output processed with Cell Ranger 5.0.1 to produce filtered feature-barcode count matrices (http://10xgenomics.com).

Single-cell analyses were performed using the Seurat package in R (v.4.1.0) (Butler et al., 2018). Count matrices filtered to retain only genes expressed in three or more cells in a sample, were used for further analysis. Cells with high mitochondrial gene percentage or in the 1st or 99th percentile of transcript counts were also removed. Initially, all sequenced cell types were analyzed together. Data were processed following standard practices, including log-normalization of UMI counts, and regression of mitochondrial gene expression. Principal component analysis was subsequently performed on the most variable genes. Cluster identification (at a resolution of 0.5) and UMAP visualization was performed on the top 20 principal components. Differential gene expression for gene-marker discovery across the clusters was performed using the Wilcoxon rank-sum test.

Subsequently, for 5FU experiments the following analyses were performed. 1) For crypt epithelial cells: *Epcam$^+$*, *Cd44$^+$* cells were identified as having expression of *Epcam* >1, *Cd44* >1 and expression of *Cdh5*, *Cd31*, *Kdr* and *Pdfgra* <1. *Myh11$^+$* cells were also excluded. 2) ECs were isolated as *Cdh5*, *Cd31*, *Kdr1* >1 and *Epcam*, *Cdh1*, *Pdgfra1* <1. EC clusters that expressed *Lyve1* were identified as LECs. 3) Mesenchymal cells were isolated as *Pdgfra* >1, *Cdh5*, *Kdr*, *Cd31*, *Epcam*, *Cdh1* <1. For each cell type, filtering, clustering, and differential gene expression testing was done as described above. For pathway analysis, WEB-GESTALT (WEB-based Gene SeT AnaLysis Toolkit) (Liao et al., 2019) was utilized, where genes that had at least a 0.5 Log2 upregulation in control LEC

vs knock-out LEC or genes that had at least a 0.5 Log2 upregulation in knock-out LECs vs. control LECs were utilized for over-representation analysis. False discovery rate (FDR)-adjusted p values of less than 0.05 were considered statistically significant.

Mucin staining

For mucin staining, the jejunum (middle third of the small intestine) was isolated 3 days after the last 5FU injection. Fragments of 1.5 cm in length containing fecal pellets were then selected and placed directly into methacarn fixative (60% methanol, 30% chloroform, 10% acetic acid). Fragments were fixed for 3 days rocking at room temperature. Following fixation, fragments were washed twice in methanol for 20 min each wash, twice in absolute ethanol for 20 min each, and twice in xylene for 10 min each. The tissue was then embedded in paraffin blocks following standard procedures and cut into 4, 7, and 14 μm sections. Sections were stained with 20 μg/mL UEA1-FITC.

mRNA extraction and RT-qPCR analysis

Tissues were collected and LECs were sorted as described above. 20,000 LECs were then resuspended in lysis buffer from the PicoPure™ RNA Isolation Kit. mRNA was extracted following the manufacturer's protocol and resuspended in 13.2uL of elution water. mRNA was then used for reverse transcription using the High-Capacity cDNA Reverse Transcription Kit. The resulting cDNA was diluted (4X) before proceeding to qPCR using TaKaRa Taq DNA Polymerase mix. Relative gene expression was calculated by using $\Delta\Delta$Ct method and normalized to $\beta2\,m$ expression. Results are displayed as mean ± s.e.m., Mann Whitney U-test, two-sided.

QUANTIFICATION AND STATISTICAL ANALYSIS

Data were assessed and analyzed using appropriate statistical methods. Mann Whitney U-test was utilized unless otherwise noted. GraphPad Prism v.9 was used for all statistical analysis, unless otherwise indicated. No statistical methods were used to determine sample size. Unless otherwise stated, the experiments were not randomized. The investigators were blinded during 5FU and DT experiment quantifications.